Bimetallic Uranyl/Cobalt(II) Isothiocyanates: Structure, Property and Spectroscopic Analysis of Homo- and Heterometallic Phases

Journal:	*Dalton Transactions*
Manuscript ID	DT-ART-05-2021-001464.R1
Article Type:	Paper
Date Submitted by the Author:	02-Jun-2021
Complete List of Authors:	Byrne, Nicole; The George Washington University, Chemistry Schofield, Mark; The George Washington University, Chemistry Nicholas, Aaron; The George Washington University, Chemistry Cahill, Chris; The George Washington University, Chemistry

SCHOLARONE™
Manuscripts

Bimetallic Uranyl/Cobalt(II) Isothiocyanates: Structure, Property and Spectroscopic Analysis of Homo- and Heterometallic Phases

Nicole M. Byrne,[a] Mark H. Schofield,[a] Aaron D. Nicholas,[a] Christopher L. Cahill[a*]

[a]Department of Chemistry, The George Washington University, 800 22nd St. NW, Suite 4000, Washington, D.C., 20052

Abstract

We report the synthesis and characterization of a family of UO_2^{2+}/Co^{2+} isothiocyanate materials containing $[UO_2(NCS)_5]^{3-}$ and/or $[Co(NCS)_4]^{2-}$ building units charged balanced by tetramethylammonium cations and assembled *via* S⋯S or S⋯O_{yl} non-covalent interactions (NCIs), namely $(C_4H_{12}N)_3[UO_2(NCS)_5]$, $(C_4H_{12}N)_2[Co(NCS)_4]$, and $(C_4H_{12}N)_5[Co(NCS)_4][UO_2(NCS)_5]$. The homometallic uranyl phase preferentially assembles *via* S⋯S interactions, whereas in the heterometallic phase S⋯O_{yl} interactions are predominant. The variation in assembly mode is explored using electrostatic surfaces potentials, revealing that the pendant -NCS ligands of the $[Co(NCS)_4]^{2-}$ anion is capable of outcompeting those of the $[UO_2(NCS)_5]^{3-}$ anion. Notably, the heterometallic phase displays atypical *blue* shifting of the uranyl symmetric stretch in the Raman spectra, which is in contrast to many other compounds featuring non-covalent interactions at uranyl oxygen atoms. A combined experimental and computational (density functional theory and natural bond orbital analyses) approach revealed that coupling of the uranyl symmetric stretch with isothiocyanate modes of equatorial –NCS ligands was responsible for the atypical *blue* shift in the heterometallic phase.

Introduction

The uranyl cation (UO_2^{2+}) is of considerable interest due to its role(s) in the nuclear fuel cycle and the potential environmental impact of uranyl-containing materials. As such, numerous studies have probed the behavior of the UO_2^{2+} cation in hybrid materials, often synthesized from aqueous and/or highly acidic media. As a result, a large, structurally diverse library of compounds such as coordination polymers and metal organic frameworks (MOFs) has emerged, providing a platform to probe further the chemistry of the uranyl cation.[1-6] Beyond the structural diversity afforded by prudent ligand selection, the uranyl is also prone to oligomerization *via* hydrolysis, leading to the formation of a rich catalog of polynuclear uranyl-containing species and multi-dimensional architectures in the solid state.[1-7] The ability to control the synthesis to promote the formation of *discrete* anionic building units, however, allows for the systematic exploration of families of related structures. Recent efforts in our group have sought to influence solid-state speciation through syntheses in low pH, high anion media to generate reproducible and monodisperse anions such as $[UO_2X_y]^{2-y}$ (X = Cl, Br, NCS).[1,6-10] Doing so thus creates an opportunity for assembly *via* non-covalent interactions (NCIs) such as hydrogen and halogen bonding, or S$^{...}$S interactions when combined with protonated organic cations. Moreover, this creates a forum to probe U=O bonding *via* tuning of equatorial ligand environments and promoting O_{yl} engagement.

The uranyl oxo atoms are often terminal and typically "off-limits" to further coordination. That said, these atoms exhibit Lewis base behavior, and are capable of serving as hydrogen bond acceptors.[11-13] Work by Hayton *et. al.*[12] and others,[11,13-16] have detailed ways to encourage participation of the –yl oxygen in coordination by appropriately pairing it with hydrogen bond donors or weak Lewis acids, which in turn weaken the U=O bond upon coordination. Additionally, it has been found that uranyl bond strength can be influenced by both equatorial and second sphere

species.[8,11,17,18] In our lab, Carter *et al.* reported the use of *halogen* bonding as a viable method for "turning-on" interactions at the -yl oxygen in uranyl benzoate complexes, at the expense of U=O bond strength.[17-19] Upon thorough investigation of this family of compounds, it was found that the presence of stronger electron-donating equatorial ligands, i.e. terpyridine over phenanthroline, "primed the pump" to activate the –yl oxygen to better accept non-covalent interactions,[19] which is consistent with other literature precedent.[16,20] Our group later revisited the uranyl benzoate system to also determine the relationship between equatorial benzoate identity and observed Raman responses, in which unexpected ligand coupling with uranyl modes prompted the emergence of an additional Raman active –yl band.[21]

A forum conducive to exploring these influences further is the homo-and heterometallic isothiocyanates reported herein. Building on the homometallic uranyl pseudohalide compounds reported by Surbella *et al.*[22,23] and others,[11,24-31] we see opportunities to introduce secondary metal centers and thus the potential to probe NCI preferences, both equatorially and axially, as well as their subsequent effect on U=O bonding. Terminal sulfur atoms on pendant –NCS ligands in particular have the ability to accept or donate NCIs.[32] As such, we report a family of materials featuring S···S, S···N, and S···O_{yl} interactions and computational treatment thereof. Differences in NCI type and identity, due to the introduction of a second metal center, alters uranyl bonding and spectroscopic properties in the resultant heterometallic phase. In particular, uranyl oxo engagement results in a *blue* shift of Raman symmetric stretching frequencies, in contrast to our previous studies.[17-19] At first glance, this would imply a *strengthening* of the U=O bond upon formation of NCIs, yet an atomic orbital level investigation using computational tools (density functional theory based frequency calculations, natural bond orbitals, and Wiberg bond orders) instead demonstrates a bond *weakening* offset by normal mode coupling of the uranyl symmetric stretch with the U-

4

NCS vibrations. Looking at these influences comprehensively, we demonstrate a limitation in using spectroscopic techniques alone to quantify relative U=O bond strengths, as the effects of normal mode coupling may, in fact, be left unaccounted for.

Experimental Methods

   Synthesis. A complete description of the synthesis of all compounds **1-7** can be found in the Electronic Supporting Information, however, a procedure for the preparation of those discussed in detail is included below. $[UO_2(CH_3COO)_2]\cdot 2H_2O$ (Fisher Scientific, 99%), $CoCl_2\cdot 6H_2O$ (Sigma Aldrich, 97%), KNCS (Fisher Scientific, 99%), and $C_4H_{12}NCl$ (Sigma Aldrich, 97%) are commercially available and were used as purchased without further purification prior to synthesis. Supramolecular assembly of **1-3** is shown in **Scheme 1**.
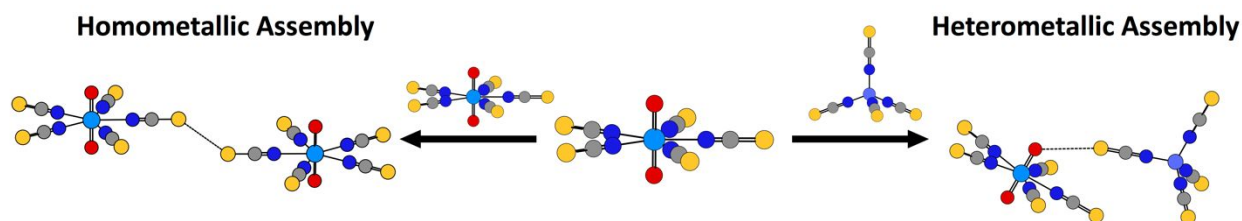
Scheme 1: Assembly schematic for uranyl isothiocyanate materials. Left: Reproducible $[UO_2(NCS)_5]^{3-}$ building units are paired with appropriate cations (not shown) to allow for S$\cdots$S interactions in the solid state. Right: $[Co(NCS)_4]^{2-}$ and $[UO_2(NCS)_5]^{3-}$ anions assemble and feature the emergence of isothiocyanate –yl interactions in the solid state.

   Homometallic U-phase: Compound 1

Caution! Although the uranium source used (uranyl acetate dihydrate $[UO_2(CH_3COO)_2]\cdot 2H_2O$) contains depleted uranium, precautions for handling radioactive materials should be followed.

As in previous studies,[1,9,10] a combination of high anion media and low pH are used to minimize hydrolysis and provide a more limited speciation profile and consequently a single uranyl species (in this case the $[UO_2(NCS)_5]^{3-}$ trianion) in the solid state. Uranyl acetate dihydrate (0.025 g, 0.059 mmol) was dissolved in 5 mL water in a 20 mL glass scintillation vial. 6 molar equivalents of potassium thiocyanate were then added (0.0343 g, 0.354 mmol), resulting in a clear, yellow solution with no apparent phase separation or cloudiness. To this solution, 4 molar equivalents of tetramethylammonium (TMA^+) were added. The pH was adjusted to approximately 4 (from 6.5) using concentrated HCl. Solutions were left open to evaporate in a fume hood at ambient temperature, until dryness was obtained. Single crystals of **1** first appeared after about four days and continued to form over the course of several more days. This phase may also be obtained *via* the (similar) synthetic procedure previously reported by Rowland *et. al.*,[25] as well as hydrothermally at 90 °C for 72 hours in a Teflon-lined acid digestion vessel, similar to **3**. Performing the hydrothermal syntheses at temperatures above 90 °C or at a pH below 3, however, results in -NCS ligand degradation, yielding a variety of sulfate salts, xanthan hydride, or octothiocane (S_8) consistent with literature reports.[33-35]

Homometallic Co-phase: Compound 2

Cobalt chloride hexahydrate (0.025g, 0.105 mmol) was dissolved in 5 mL H_2O. To this solution, 6 molar equivalents of potassium thiocyanate were added (0.0613 g, 0.630 mmol), as well as 3 molar equivalents of TMA^+. The reaction was carried out in a 20 mL glass scintillation vial and left open to slowly evaporate at room temperature in a fume hood until reaching dryness, with crystals forming rapidly over the course of several hours. This phase may also be prepared using the synthesis presented by Shurdha *et. al.*.[36]

Heterometallic phase: Compound 3

5 mL of water were added to a 23 mL Teflon-lined Parr acid digestion vessel, to which uranyl acetate hydrate (0.025 g, 0.059) was added, along with an equimolar amount of cobalt chloride. 12 molar equivalents of potassium thiocyanate (0.0687 g, 0.707 mmol) were then added to the reaction vessel, followed by 5 molar equivalents of TMA$^+$. The pH was adjusted to approximately 4 with concentrated HCl. The vessel was sealed and heated at 90 ºC for 72 hours under autogenous pressure, then cooled to room temperature under ambient conditions before opening. The resultant solution was transferred into a petri dish, and allowed to evaporate to dryness at room temperature where single crystals of **3** formed over the course of days. Room temperature syntheses did not produce diffraction quality single crystals and instead resulted in either phase separation. In the heterometallic synthesis, it appears as though the reaction is more sensitive to the influence of pH and temperature, and is more likely to form unwanted side-products.

X-ray Structural Determination. Single crystals from each reaction were isolated and mounted on 20 μm MiTeGen micromounts. Reflection data were collected using 0.5°ω and φ scans at 100(2) K. Data were collected on a Bruker D8 Quest equipped with a Photon II detector, using a Mo Kα source. The APEX III software suite[37,38] was used for integrating the data then performing an absorption correction, which incorporates both SAINT[39] and SADABS.[40] In the case of minor twinning, as seen in **2**, TWINABS[41] was used to handle the absorption correction of both components. All structures were solved by SHELXL-16[42,43] using direct methods, within the APEXIII program. The Olex2[44,45] software package, in conjunction with SHELXT,[42] were used for structural refinements which were later visualized and analyzed in Mercury.[46] All non-hydrogen atoms were located using Fourier difference maps and refined anisotropically. Hydrogen

atoms were placed in ideal locations using HFIX33 for methyl groups, and HFIX43 for aromatic hydrogen atoms, allowing hydrogen atoms to ride on their parent atoms. After the final refinement, CrystalMaker 8.2.2 was used to produce structural figures.[47]

PXRD. Powder X-ray diffraction (PXRD) was performed on bulk samples of **1-7** to determine phase purity and reproducibility. Collections were taken on a Rigaku Miniflex (Cu Kα = 3-60°), evaluated with the Match! software program,[48] and are provided in the Electronic Supporting Information (**Figures S8-S13**). These unoptimized synthesis conditions for **1-7** resulted in impure products, often containing a combination of desired phases with the metathesis products of starting materials.

Spectroscopic Analysis. UV-Visible diffuse reflectance spectroscopy (UV-Vis-DRS) was performed on separated crystals of compounds **1-3**. Solid-state spectra were collected at room temperature using a Mikropack DH-2000-BAL deuterium and halogen light source coupled with an Ocean Optics Flame detector. Scattered light was collected with a fiber optic cable attached to a manual microprobe, allowing for non-destructive spectral collection. $BaSO_4$ was used as a reference material for calibration. After spectra collection, data was processed using the OceanView spectroscopy software package. Raman spectra of single crystals of U-containing phases **1** and **3** were collected using a HORIBA LabRAM HR Evolution Raman Microscope over the 150-3,000 cm^{-1} range. An excitation line at 532 nm was used for each collection, at 10 accumulations for 4-6 seconds depending on sample intensity. Gaussian fits of Raman peaks were generated using the Fityk software suite.[49] Infrared spectra of single crystals of **1** and **3** were collected from 650-2400 cm^{-1} using a Perkin Elmer Frontier spectrometer with an ATIR attachment. Collections were taken over 16 accumulations using a 0.50 cm^{-1} step. All spectra are provided in the Electronic Supporting Information (**Figures S14-S18**, **S19-S20**).

8

Computational Methods. Density functional theory (DFT) calculations were performed using Gaussian16[50] and NBO7[51] on the high performance computing cluster at The George Washington University. Atomic coordinates were taken from crystallographic data. Geometry optimization, frequency calculations, and NBO analyses[52,53] were performed using the B3LYP functional with the following basis sets: def2TZVP for Co, N, C, S, and O, and the effective core potential ECP60MWB_SEG basis set for U was used and paired with the ECP60MWB pseudopotential.[54-56] Method validation was performed across the BLYP, CAM-B3LYP, M062X, and TPSSH functionals (**Tables S20-S21**). Electrostatic surface potential (ESP) plots were generated using Gaussview 6.0[57] at a 0.002 isovalue, with ranges set appropriate to each anion. Geometry optimized ground state structures of monomeric $[UO_2(NCS)_5]^{3-}$ and $[Co(NCS)_4]^{2-}$ visualizing the HOMO and LUMO were rendered in Avogadro (**Figures S22-S23**).[58,59] Figures of pertinent orbital interactions from NBO analysis were generated using the Jmol java applet, in combination with the Jmol visualization helper functionality (**Figures S29-S32**).[60] All figures and tables were generated using the B3LYP outputs.

Results and Discussion

Crystal Structures. The $[UO_2(NCS)_5]^{3-}$ anion is common to **1** and **3,** and features a linear, triatomic uranyl coordinated equatorially by five linear isothiocyanate ligands to form a pentagonal bipyramidal geometry (**Figure 1**). This anion features an average bond distances of U=O 1.766 Å, U-N 2.449 Å, N=C 1.153 Å, and C=S 1.627 Å. Subtle variations in the anion exist between each compound, with occasional deviation of isothiocyanate ligands from the equatorial plane.
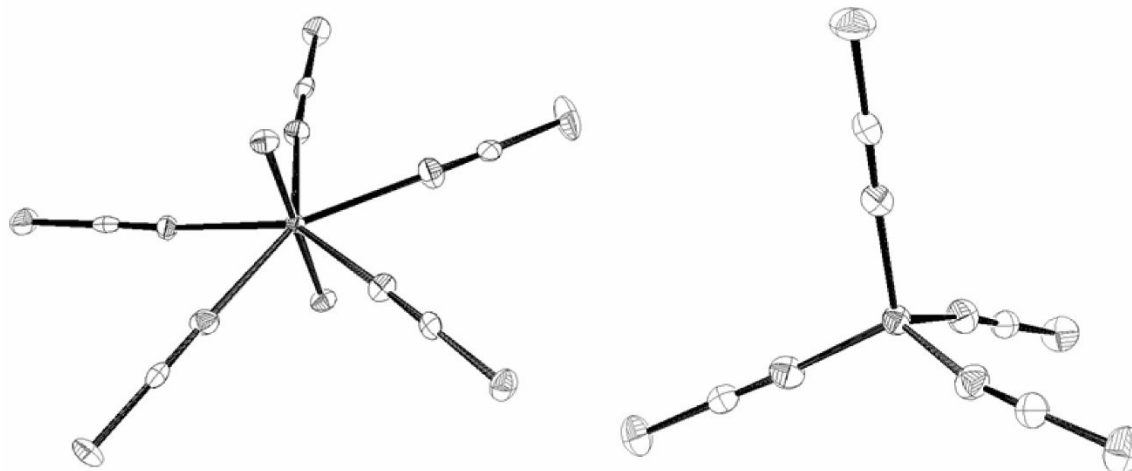
Figure 1: Left: ORTEP plot of the $[UO_2(NCS)_5]^{3-}$ anion from **1**. The uranyl is bound equatorially by five isothiocyanate ligands to form the trianion of pentagonal bipyramidal geometry. Right: ORTEP plot of the $[Co(NCS)_4]^{2-}$ dianion from **2**. The $[Co(NCS)_4]^{2-}$ anion features a Co(II) ion coordinated by four isothiocyanate ligands in a tetrahedral geometry.

The $[Co(NCS)_4]^{2-}$ dianion is present in **2** and **3** and features a central Co(II) coordinated by four nitrogen-bound isothiocyanate ligands in a tetrahedral geometry (**Figure 1**), consistent with literature findings.[36,61-64] The average Co-N bond distance in **2** and **3** is 1.954 Å, with average N=C distances being 1.158 Å, and C=S distances being 1.618 Å. Again, subtle differences exist between each $[Co(NCS)_4]^{2-}$ dianion, with slight distortion of the tetrahedral geometry. Unsurprisingly, owing to hard-soft acid-base theory,[32] in both uranyl and cobalt phases, thiocyanate ligands are coordinated through the nitrogen end of the ambidentate –NCS ligand, leaving the S-terminus free for participation in non-covalent interactions.

When considering the assembly of isothiocyanate containing species, interactions between ligands can be explained, to a limited extent, using the polarization model.[65] As a consequence of the –NCS bonding to either metal, an asymmetric polarization of electron density at the terminal end leads to the formation of a partially positively charged "cap," also known as a σ-hole, and a partially negatively charged "belt" perpendicular to the bonding axis of the ligand. This is

consistent with findings made by Surbella *et al.*,[8] who noted the non-bonding S $3p$ orbitals were responsible for the formation of the negative belt surrounding the periphery of the ligand. This allows for the formation of two types of interactions, both of which occur in supramolecular assembly (**Scheme 2**).[32,65-69] Type I interactions feature a staggered head-on geometry and typically arise from packing, and therefore are not considered structure-directing. Type II, however, involves a side-on interaction between the positive σ-hole on the S-terminus of one anion and the negative belt along another to form a strong, structure-directing interaction (**Scheme 2**).[65-69] Like hydrogen and halogen bonding, these typically weak interactions can be strengthened by charge or resonance assistance effects, leading to interaction energies up to hundreds of kJ/mol.[69] Moreover, the materials targeted herein incorporate tetramethylammonium (TMA$^+$) cations, which are not expected to participate in meaningful NCIs, since we aim to minimize the interference of (potentially) coordinating countercations, instead focusing on the role of NCIs provided by the − NCS ligands.
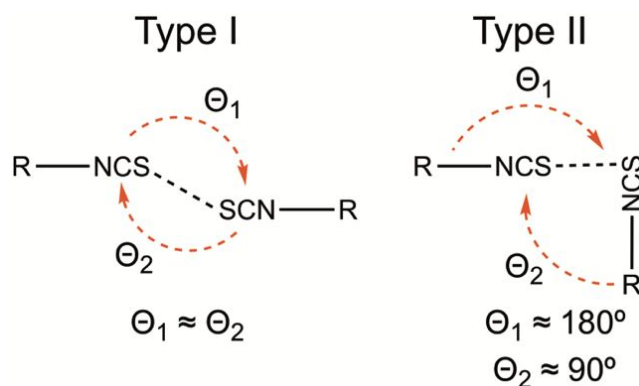
Scheme 2: Typical chalcogenide interaction motifs, adapted from Cavallo *et al.*[65]

Structural Descriptions of Compounds 1-3

Compound 1 (C$_4$H$_{12}$N)$_3$[UO$_2$(NCS)$_5$]: Compound **1** was previously reported,[25] yet a new data collection was performed to ensure comparative consistency across compounds. Compound **1**

crystallizes in the P2$_1$/c space group, and is comprised of the $[UO_2(NCS)_5]^{3-}$ anion charge balanced by three crystallographically unique TMA cations. In **1**, isothiocyanate ligands deviate substantively from the equatorial plane (**Figure 2**). Within the unit cell of **1**, the average S⋯S distances between –NCS ligands are above 3.8 Å, with the shortest interaction at Σr_{vdW} = 3.590(1) Å, corresponding to 99.7% of the sum of the van der Waals (vdW) radii.[70] This interaction is best defined as a Type I interaction, with θ_1 = 132.4° between two adjacent S atoms, and allows for the formation of dimers along the *c*-axis (**Figure 2**).
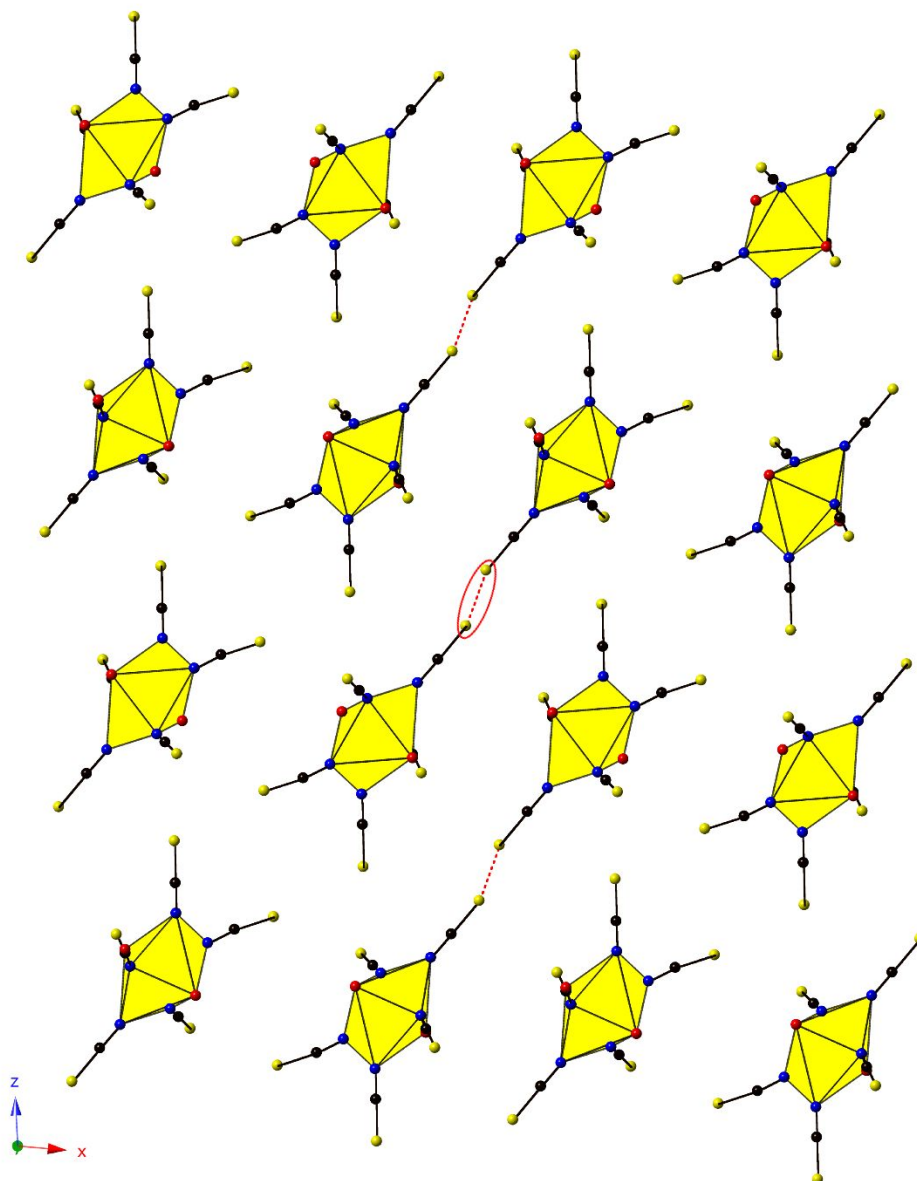
Figure 2: Packing of **1** shown down the *b*-axis to highlight head-on S···S interactions between two adjacent anions. Uranyl polyhedral are shown in yellow; N, S, and O are shown as blue, yellow, and red spheres, respectively.

Compound 2 (C₄H₁₂N₃)₂[Co(NCS)₄]: Compound **2** was previously reported from room temperature powder data,[36] yet a low temperature single crystal data set was collected for appropriate comparison across this family of materials. In addition, our refinement produced a model which contrasts with the original report and points to a P-1 structure with pseudo-

merohedral twinning that emulates monoclinic symmetry. The average S⋯S interaction present in

2 is above 4.0 A, with the closest being Σr_{vdW} = 4.006(1) Å, considerably outside the vdW radii at

111.3% vdW. There are, however, several close C=S⋯N=C interactions of Type II (θ_2 = 87.62°)

present at Σr_{vdW} = 3.304(3) Å, which corresponds to a 98.6% vdW (**Figure 3**). The existence of

S⋯N interactions allows for the formation of pseudo-chains which propagate along the b-axis, with

the TMA$^+$ situated in between.
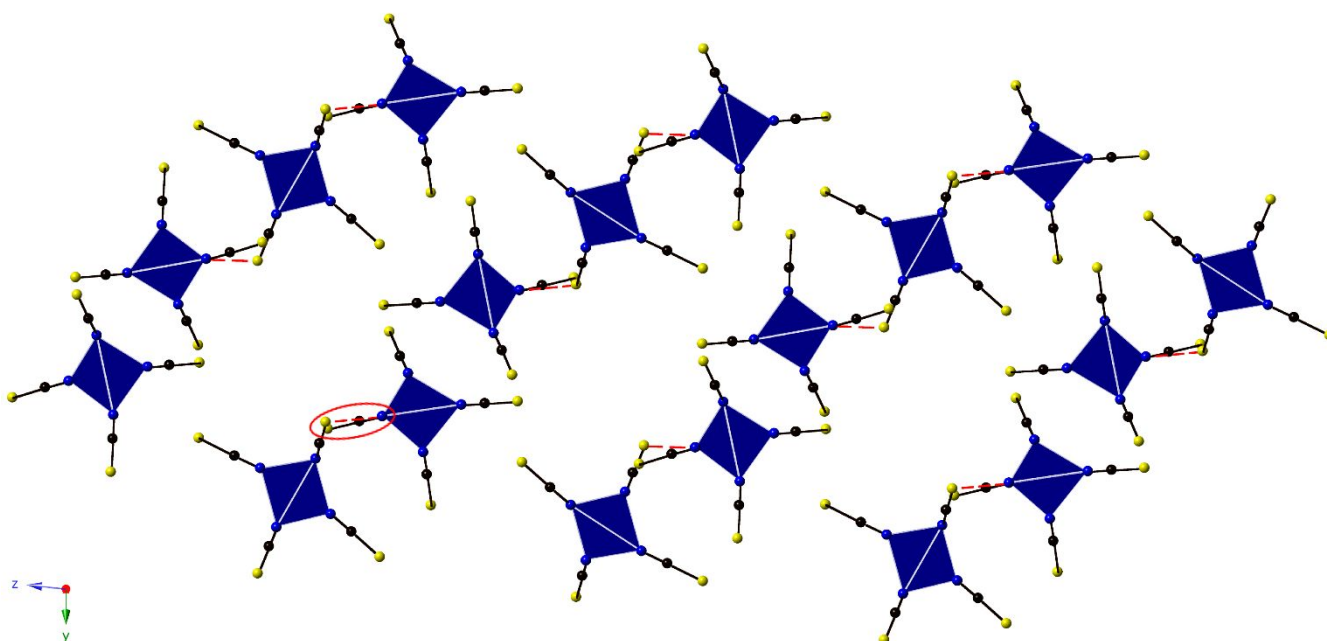
Figure 3: Compound **2** down the *a*-axis showing the pseudochains formed by the packing of
$[Co(NCS)_4]^{2-}$ dianions as a result of weak S⋯N interactions. Cobalt atoms are shown as blue
polyhedra; N and S shown as blue and yellow spheres, respectively.

Compound 3 $(C_4H_{12}N)_5[UO_2(NCS)_5][Co(NCS)_4]$: Compound **3**, reported here for the first

time, crystallizes in the space group P2$_1$/c, and contains unique $[UO_2(NCS)_5]^{3-}$ and $[Co(NCS)_4]^{2-}$

anions, charge-balanced by five TMA$^+$ cations. No notable S⋯S interactions exist between

adjacent anions in the structure, with the closest S⋯S contact at Σr_{vdW} = 3.650(3) Å, which

corresponds to a 101.49% vdW overlap. Of particular interest, however, is the interaction between

a pendant S atom on a $[Co(NCS)_4]^{2-}$ anion and a uranyl oxygen atom with an interaction distance of $\Sigma r_{vdW} = 3.188(3)$ Å, which corresponds to a 96.0% vdW overlap (**Figure 4**). The geometry of this interaction can be best described as Type II ($\theta_1 = 171.1(1)°$, $\theta_2 = 129.2(2)°$), suggestive of a structure-directing role as opposed to merely a consequence of packing.
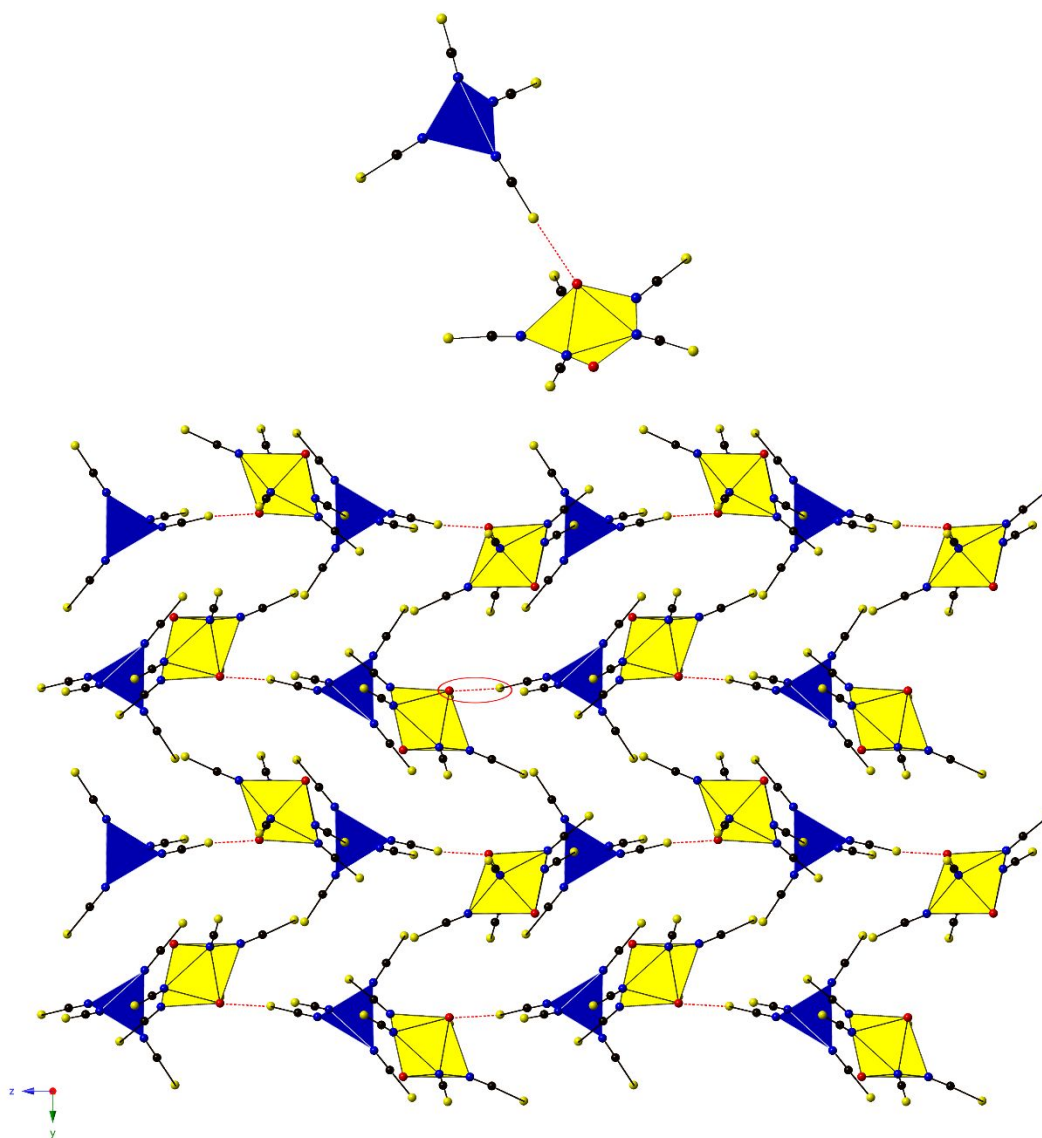
Figure 4: Top: Selected portion of **3** shown to highlight the $S \cdots O_{yl}$ interaction present. TMA cations excluded to highlight the prominent $S \cdots O_{yl}$ interaction. Bottom: Packing of **3** down the a-axis to show anions held together by $S \cdots O_{yl}$ interactions. Uranyl polyhedra are shown in yellow, cobalt polyhedra are shown in blue, and N, S, and O are shown as blue, yellow, and red spheres, respectively.

Additional phases **4-7** synthesized while exploring this compositional space can be found in the Electronic Supporting Information, along with details relating to data collection and structural refinements. These phases pair the $[UO_2(NCS)_5]^{3-}$ and $[Co(NCS)_4]^{2-}$ anions with cesium, $Cs_9[Co(NCS)_4]_4(NCS)$, tetraethylammonium (TEA$^+$), (TEA$^+$)$_2$[UO$_2$(NCS)$_4$(H2O)]·H$_2$O, and pyridinium (Py$^+$) cations, (Py$^+$)$_3$[UO$_2$(NCS)$_5$]·H$_2$O,Py, as well as a TMA$^+$ polymorph that formed as a minor side-product of **1**, (TMA$^+$)$_3$[UO$_2$(NCS)$_5$]. In all phases, similar bonding motifs are observed to those described above. No other heterometallic phases were observed, highlighting the fact that the countercation likely plays a role in the assembly motifs observed in the solid state, as a heterometallic phase was observed *only* with TMA$^+$. It is important to note, however, that S$^{...}$O$_{yl}$ interactions are only present in **3** and in none of the supplemental phases.

Electrostatic Surface Potentials and Supramolecular Assembly. Calculating the values of electrostatic potential along an isosurface of both the $[UO_2(NCS)_5]^{3-}$ and $[Co(NCS)_4]^{2-}$ anions allows one to identify candidate NCI donor and acceptor sites in a crystal structure,[71-74] with a goal of rationalizing assembly motifs. As such, we have calculated ESP surfaces for both anions found in **1-3** (**Figure 5**). The best donor region of a molecule occurs where the potential is most positive (or least negative in the case of an anion), and for $[UO_2(NCS)_5]^{3-}$, is found at the S-terminus of the –NCS ligand with a value -657 kJ/mol. The best acceptor region on an anion has the most negative ESP value and is found close to the bound N, at -885 kJ/mol. Owing to steric hindrance however, this site is inaccessible for participation in NCIs, which therefore leaves the uranyl oxo (-856 kJ/mol), as the best available acceptor site. As such, the S-terminus and O$_{yl}$ are the best donor and (accessible) acceptor, respectively, meaning assembly *via* S$^{...}$O$_{yl}$ interactions

should be present in homometallic phases. This logic has held true in other many other solid state organic compounds[74,75] and indeed in more related uranyl systems.[3,6-11]
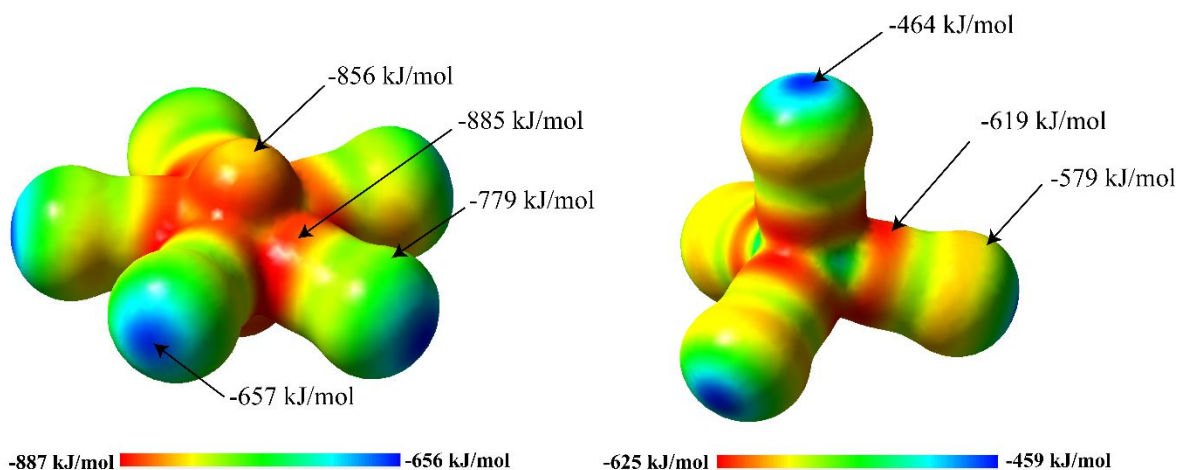
Figure 5: Left: Electrostatic surface potentials on a 0.002 au isosurface from the $[UO_2(NCS)_5]^{3-}$ anion. Right: Electrostatic surface potentials on a 0.002 au isosurface of the $[Co(NCS)_4]^{2-}$ anion. The color scheme represents magnitude of ESP at specific points along the isosurface. Areas of highest and lowest surface potential are shown blue and red, respectively.

Contrasting this thinking, however, is homometallic phase **1**, where the $[UO_2(NCS)_5]^{3-}$ anions are linked via weak $S^{...}S$ interactions, with a 99.7% vdW overlap. These interactions are Type I, likely the result of packing, as opposed to assembly directing. Kusamoto[67] and others[23,68,69] observed similar intermolecular interactions, which were deemed attractive but weak. And whereas our countercations were selected owing to their *inability* to participate in NCIs, it would appear that their presence is not innocent in terms of influencing assembly, and perhaps there is a meaningful contribution from coulombic attraction between the cation and the negative O_{yl} region.

Turning to the $[Co(NCS)_4]^{2-}$ anion, the best donor is again the σ-hole on the pendant S, at -464 kJ/mol, with all –NCS ligands being approximately equivalent. The best acceptor region is at the N of the bound –NCS ligand, at -619 kJ/mol which is sterically accessible for forming interactions. Consequently, compound **2** exhibits best donor-acceptor interaction pairs, in which Type II $S^{...}N$ interactions are observed, with a vdW overlap of 98.6%.

When both anions are present in the system, as in heterometallic **3**, the best relative donor and acceptors are no longer found on the same anion which in turn allows for the formation of new NCIs not observed in **1** and **2**. The σ-hole on Co-NCS ligands remains the best donor, again at -464 kJ/mol, whereas the best accessible acceptor site is the –yl oxygen, at -856 kJ/mol. As a consequence, $S{\cdots}O_{yl}$ interactions emerge at the expense of $S{\cdots}S$ or $S{\cdots}N$ NCIs. A summary of NCIs observed in **1-3** is shown in **Table 1**.

Table 1: Summary of predominant NCIs present in **1-3**, with relevant interaction type, ESP values of best acceptor/donor regions, and strength of interaction as a function of % van der Waals radii.

Compound	Predominant NCI	Type	ESP Values (kJ/mol)		% vdW overlap
			Donor	Acceptor	
1	S⋯S	I	-657	-779	99.7%
2	S⋯N	II	-464	-619	98.6%
3	S⋯O	II	-464	-841	96.0%

UV-Vis Absorption Spectral Studies. To probe the electronic structure in **1-3**, diffuse reflectance spectra were obtained from single crystals at 298 K (**Figure 6, Figure S14-S16**). Homometallic uranyl compound **1** displays strong absorption bands in the UV and high energy visible region with absorption edges of 470 nm and 430 nm, respectively. These bands are typical of uranyl containing species and have been reported extensively in the literature as a low energy $O_{yl}{\rightarrow}U$ ligand to metal charge transfer (*axial*-LMCT) overlapped with a higher energy NCS→U ligand to metal charge transfer (*equatorial*-LMCT).[23-26] Compound **2**, containing only the $[Co(NCS)_4]^{2-}$ unit, displays a UV band at 350 nm and 390 nm, as well as a visible absorption band at 700 nm and 680 nm, respectively. The $[Co(NCS)_4]^{2-}$ UV band corresponds to a $\pi{\rightarrow}\pi^*$ transition, whereas the visible band above 680 nm arises from the Co(II) d→d transition in a tetrahedral coordination environment.[36,76-78] These transitions are characteristic of $[Co(NCS)_4]^{2-}$ compounds

and responsible for the blue color of **2**.[76,78] The combination of yellow $[UO_2(NCS)_5]^{3-}$ and blue $[Co(NCS)_4]^{2-}$ building units in the solid state, perhaps unsurprisingly, results in the green color of the heterometallic compound **3**. In **3**, the uranyl *axial*-LMCT band, overlapping that of the $[Co(NCS)_4]^{2-}$ in **1**, undergoes a red shift of the absorption edge to 500 nm. Additionally, the Co(II) d→d transition, previously at 700 nm, is blue shifted to 680 nm.
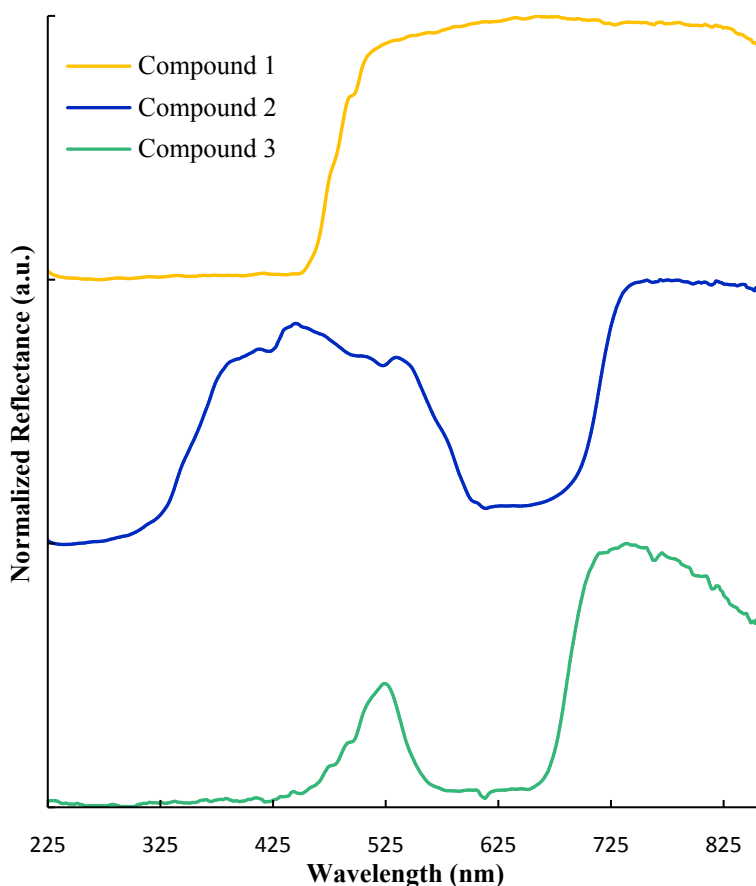
Figure 6: Normalized diffuse reflectance spectra of **1-3** at 298 K.

As the absorption spectra of uranyl complexes are highly dependent on the coordination environment about the metal center, shifts in band energies can provide information, in this case, on perturbation of the $[UO_2(NCS)_5]^{3-}$ unit when both anions are present. The *red shift* of the uranyl

band to lower energies in **3** is indicative of weakening of the U=O bond upon formation of $S \cdots O_{yl}$

interactions, consistent with our previous work surrounding oxo interactions.[17-19]

Raman Spectra of Uranyl Containing Phases. The Raman-active uranyl symmetric

stretching frequency (ν_1), typically found between 750 and 900 cm^{-1}, is often used as a relative

measure of U=O bond strength.[79-83] Shifting of the ν_1 frequency within this range is usually

correlated to changes in equatorial coordination[81] and/or NCIs.[14,23,79] Enhanced equatorial ligation

in the first sphere tends to weaken the U=O bond, typically lowering the energy of, i.e. *red shifting,*

the U=O stretch. Coordination of second sphere species to equatorial ligands, in contrast, causes a

removal of electron density from the equatorial plane which is expected to strengthen the U=O

bond, causing the ν_1 frequency to *blue shift*. When NCIs directly involve the uranyl oxo, however,

opposite shifts are expected. For example, when halogen bonding at the uranyl oxo was observed

by Carter *et al.*, the symmetric stretch *red shifted*, indicating a weakening of the U=O bond likely

as a result of halogen lone pair donation to U=O σ and π antibonding orbitals.[17-19]

For this reason, the Raman spectra for compounds **1** and **3** (**Table 2**, **Figure S17-S18**) provide

an attractive opportunity for systematically probing response of the uranyl symmetric stretch to

the coordination environment. The Raman active (ν_1) stretch in compound **1**, which features only

weak S⋯S interactions and no oxo engagement, is found at 826 cm^{-1}. When $S \cdots O_{yl}$ interactions are

present however, as in **3**, we note an unexpected *blue* shift in the ν_1 to 841 cm^{-1} as well as the

emergence of an additional band at 810 cm^{-1} (**Figure 7**). This behavior is in direct contrast to

previously reported systems *vide supra* and our understanding of U=O bonding upon oxo

engagement, which makes a molecular orbital level understanding of its origin of particular

interest.

Table 2: Summary of U=O ν_1 stretching frequencies for uranyl containing compounds.

Compound	Uranyl Stretch (cm^{-1})
1	826
3	841
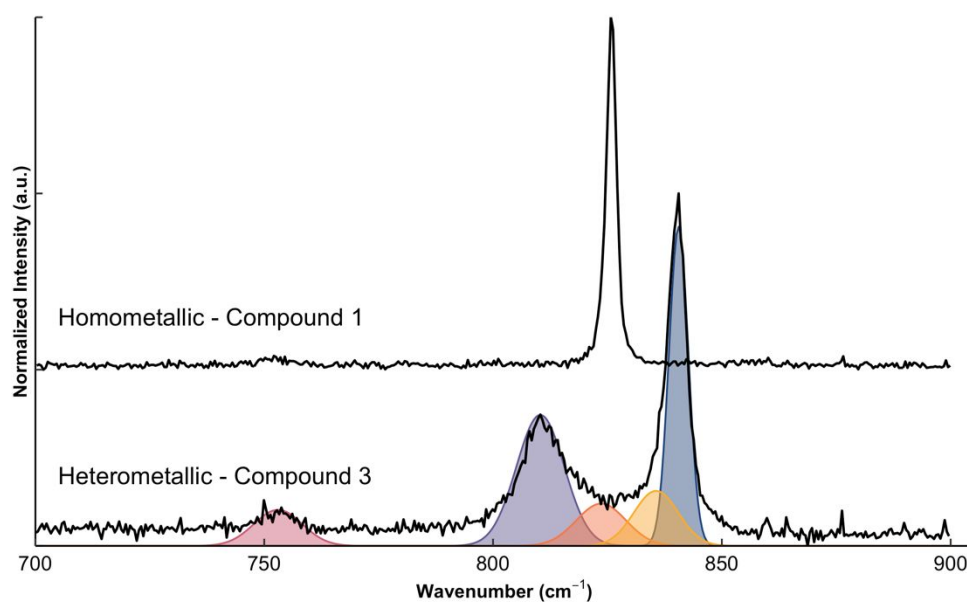
Figure 7: Raman spectra of **1** and **3**, highlighting the blue shift in the ν_1 upon formation of $S \cdots O_{yl}$, and loss of $S \cdots S$ interactions in the heterometallic phase (**3**).

Typically, a single band is observed in the 750-900 cm^{-1} region of uranyl-containing compounds as only the symmetric stretching mode (ν_1) is Raman active. However, recent work from our group has shown that select equatorial ligand normal modes can couple with the ν_1 U=O stretch[21] which manifests as an enhancement of the coupled ligand band intensities. In such cases, coupling is particularly strong when the two normal modes, which transform as the same representation, are close in energy. In $[UO_2(NCS)_5]^{3-}$, the symmetric C-S stretch (A_1' in D_{5h}) occurs at ca. 820 cm^{-1}, while the ν_1 in U=O (also A_1') is observed at ca. 900 cm^{-1}. Interaction between these modes can potentially lead to a blue shift in ν_1. As the influence of coupling would contradict the influence on electronic structure caused by NCIs, we applied a hybrid approach incorporating

DFT analysis with our experimental results to determine the origin of our blue shift. In doing so, we also needed to rule out the influence of other phenomena, *i.e. changes to U=O bond strength causing v_1 shifts*, and determine if the criteria for coupling of normal modes were met.

Computational Probe of Uranyl Electronic Structure and Bonding. A deeper understanding of S⋯O_{yl} interactions is necessary to (a) reconcile our observed blue shift in Raman stretching frequencies versus a red shift of our uranyl absorption edge and (b) place these observations in the broader context of oxo engagement efforts writ large.[13-21] Therefore, an orbital level understanding of NCIs and their influence on electronic structure and bonding is required to rationalize this atypical behavior. To accomplish this, DFT based frequency calculations and NBO analyses were performed on two XRD derived dimeric models; one homometallic UO_2^{2+} system (Model A) containing S⋯S interactions and one heterometallic UO_2^{2+}/Co^{2+} system (Model B) containing S⋯O_{yl} interactions (**Figure 8**). Frequency calculations were used to identify the energies and vibrational modes of the experimentally observed Raman bands as well as determine how substitution of S⋯S interactions for S⋯O_{yl} interactions changes the vibrational spectra. NBO calculations, and subsequent second order perturbation theory (SOPT), were used to deconstruct the atomic and molecular orbitals involved in noncovalent interactions and delineate the identity of the acceptor/donor orbitals, and percent contribution of U/O atomic orbitals in the U=O bonds.
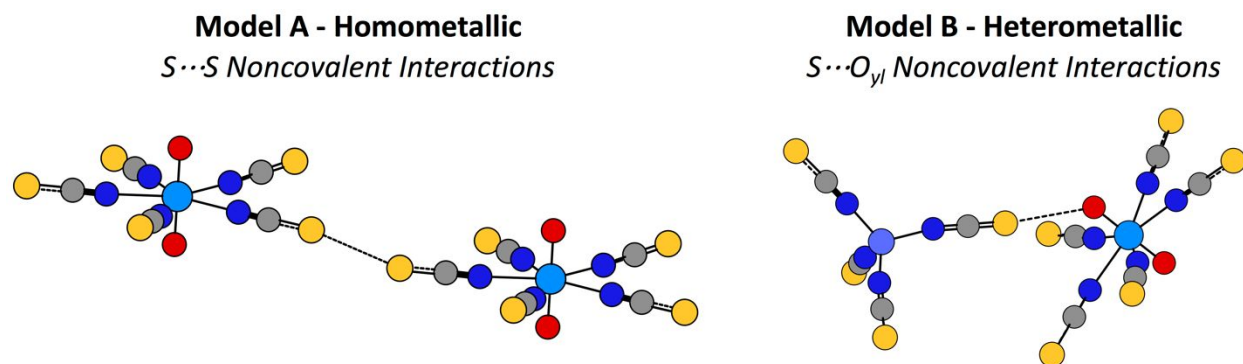
Figure 8: Left: Homometallic $[UO_2(NCS)_5]_2^{6-}$ model exhibiting S$\cdots$S interactions between uranyl units. Right: Heterometallic $[(Co(NCS)_4)(UO_2(NCS)_5)]^{5-}$ model exhibiting S$\cdots$O$_{yl}$ interactions between $[UO_2(NCS)_5]^{3-}/[Co(NCS)_4]^{2-}$ units. NCIs of interest are denoted by dashed lines.

Frequency Calculated Vibrational Modes. DFT frequency calculations on dimeric models produce the Raman spectra in **Figure 9** and are in good qualitative agreement with experimental results. Full spectra rendered from these calculations can be found in the Electronic Supporting Information (**Figure S19**), along with their atomic displacements (**Table S10-S11, video 1 and 2**). A single Raman active U=O band is observed in the *homometallic* $[UO_2(NCS)_5]_2^{6-}$ model, appearing at 925 cm^{-1}. This band, as with the experimental Raman measurements, is split in the *heterometallic* $[(Co(NCS)_4)(UO_2(NCS)_5)]^{5-}$ model, appearing at 867 cm^{-1} and 877 cm^{-1}. In the case of the homometallic model, the Raman band at 925 cm^{-1} can be described as a relatively 'pure' symmetric U=O stretch, without significant contribution from other vibrational modes. The same cannot be said of the *hetero*metallic bands whose expected U=O symmetric stretch contains significant contributions from adjacent C=S and U-N stretching on the $[UO_2(NCS)_5]^{3-}$ unit. The involvement of -NCS vibrational modes in the heterometallic uranyl stretch provides clear evidence towards coupling being responsible for the observed Raman shift, a phenomenon we have observed and reported in other uranyl species.[8,22]
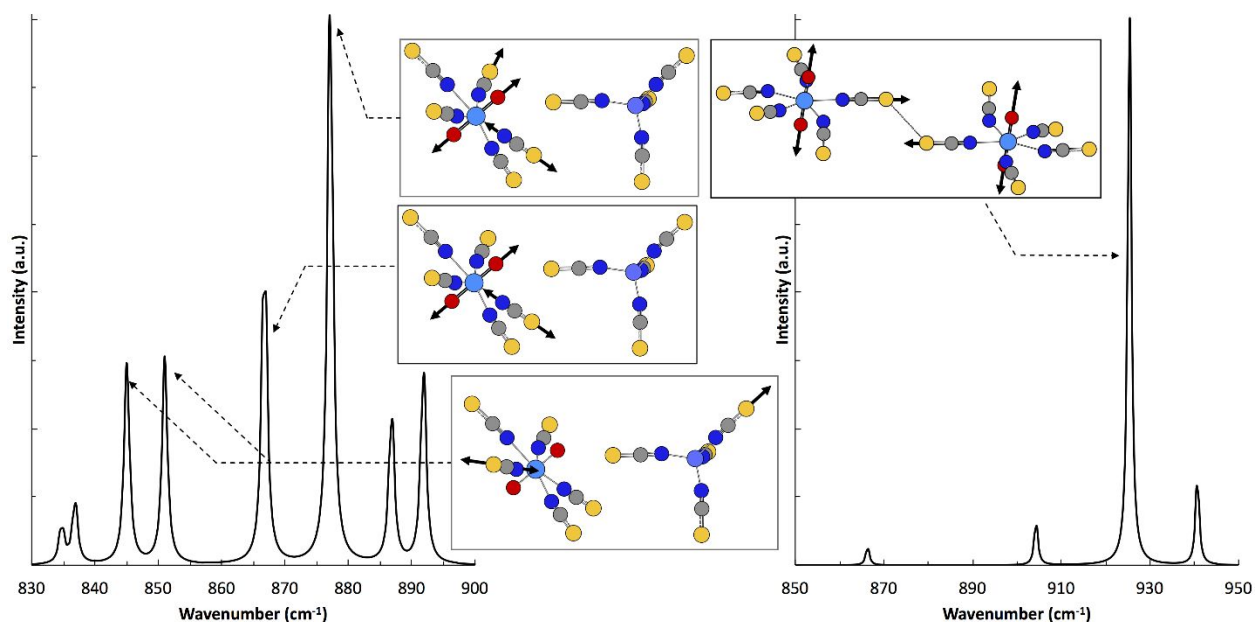
Figure 9: B3LYP calculated Raman spectra of (left) *heterometallic* $[(Co(NCS)_4)(UO_2(NCS)_5)]^{5-}$ and (right) *homometallic* $[UO_2(NCS)_5]_2^{6-}$ models. Insets show dominant atom displacement vectors of the Raman active vibrational mode.

As we have discussed above, the coupling of two vibrational modes (in this case U=O and NCS) occurs when two criteria are met: 1) the vibrational mode energies are similar and 2) the vibrational modes are of the appropriate symmetry. As such, frequency calculations of the individual monomeric $[UO_2(NCS)_5]^{3-}$ and $[Co(NCS)_4]^{2-}$ building units were performed to assess whether the criteria for coupling were met. For $[UO_2(NCS)_5]^{3-}$ the U=O and U-NCS stretches were found at 836 cm^{-1} and 782 cm^{-1}, respectively, whereas the NCS stretch in $[(Co(NCS)_4)^{2-}]$ occurred at 804 cm^{-1}. As the energy of the U=O vibration is in a similar range to the –NCS stretches found in *both* the $[UO_2(NCS)_5]^{3-}$ and $[(Co(NCS)_4)]^{2-}$ models, it can be said that the energetic criteria for vibronic coupling is thus satisfied. Analysis of the atomic displacement for these stretches demonstrates that both modes are also of the appropriate symmetry and thus meet the final criteria for successful coupling. This frequency analysis suggests that normal mode coupling is most likely responsible for the atypical blue shift of the U=O stretch, yet it fails to explain why it occurs

exclusively in the *hetero*metallic compound and involves only the U-NCS stretch and not the Co-NCS stretch in the heterometallic compounds. Presumably, the Co-NCS stretches in the heterometallic systems also are appropriate in energy and symmetry for successful coupling, yet this phenomenon is not observed in these cases. This leads us to believe that the introduction of $[Co(NCS)_4]^{2-}$ in some way modulates or encourages U=O/U-NCS coupling via second sphere $S{\cdots}O_{yl}$ noncovalent interactions.

Second Order Perturbation Theory. To assess the coupling behavior initially observed in the frequency calculations and evaluate the differences in atomic orbitals involved in the $S{\cdots}S$ and $S{\cdots}O_{yl}$ interactions in the $[UO_2(NCS)_5]_2^{6-}$ and $[(Co(NCS)_4)(UO_2(NCS)_5)]^{5-}$ models, respectively, we have invoked natural bond orbital based second order perturbation theory (SOPT) calculations. Based on the frequency calculations on homometallic $[UO_2(NCS)_5]_2^{6-}$ model it is clear that U=O and U-NCS coupling is negligible in the absence of $S{\cdots}O_{yl}$ interactions (above), yet such calculations do not provide an atomic orbital level reasoning for this observation. NBO based SOPT calculations, however, determines the identity of the donor and acceptor atomic orbitals involved in relevant NCIs and is capable of highlighting how NCIs may reorganize (for example) the nature of the charge transfer between ionic species.

In the case of homometallic Model A, $[UO_2(NCS)_5]_2^{6-}$, NBO calculations reveal that $S{\cdots}S$ interactions induce charge transfer of electrons between adjacent $[UO_2(NCS)_5]^{3-}$ anions through lone pair donation from one S to the C-S σ* acceptor orbital on the opposite –NCS ligand (**Figure 10, Table S13**). This charge transfer is bidirectional, connecting terminal S atoms of adjacent anions and is typical for chalcogen bonded species.[22,32] Crystallographically, no changes in C=S or C=N bonds are observed in the **1**. We do, however, observe a red shift of the IR stretching frequency of the C=N stretch, along with a decrease in its Wiberg bond index, which is consistent

with previous findings,[26] and results from introduction of the S⋯S interaction. Importantly, this interaction excludes any atomic or molecular orbitals involved in U=O bonding (i.e. U=O σ or U=O π bonding or antibonding orbitals) and thus should not directly affect the U=O bonding or subsequent spectroscopic properties.
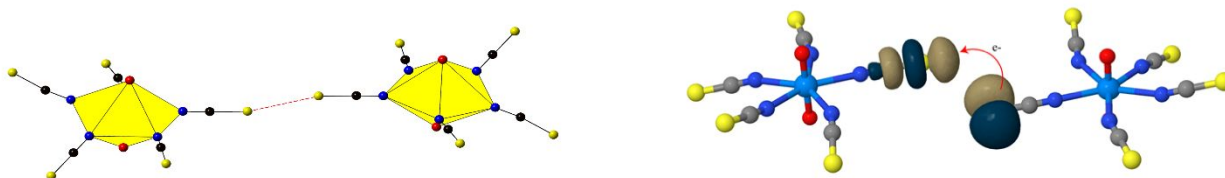
Figure 10: Left: Observed S⋯S interaction in **1** and **4.** Right: Natural localized molecular orbitals (NLMOs) involved in the S⋯S interaction, in which S lone pairs are donated to acceptor S-C σ* on the adjacent anion. An opposite, yet equivalent donation occurs in the reverse direction as well, delocalizing the equatorial π-system across the uranyl equatorial plane of both anions (**Figures S29-S30, Table S13**).

Introduction of S⋯O$_{yl}$ interactions in the heterometallic model (**Figure 11**) reveals that the atomic orbitals involved in NCIs are lone pairs on a pendant S (donor) of the [Co(NCS)$_4$]$^{2-}$ dianion and the U=O σ* orbital (acceptor) (**SI Table S14**). The net donation of electrons to a U=O antibonding orbital should be expected to *weaken* the uranium-oxygen bond, *red-shifting* its symmetric stretch frequencies, as U=O bonding orbitals are depopulated and antibonding orbitals are populated. This is consistent with our UV-Vis-DRS results (**Figure 6**), the calculated Wiberg bond indices below, as well as the findings of Carter *et. al.*.[17-19]
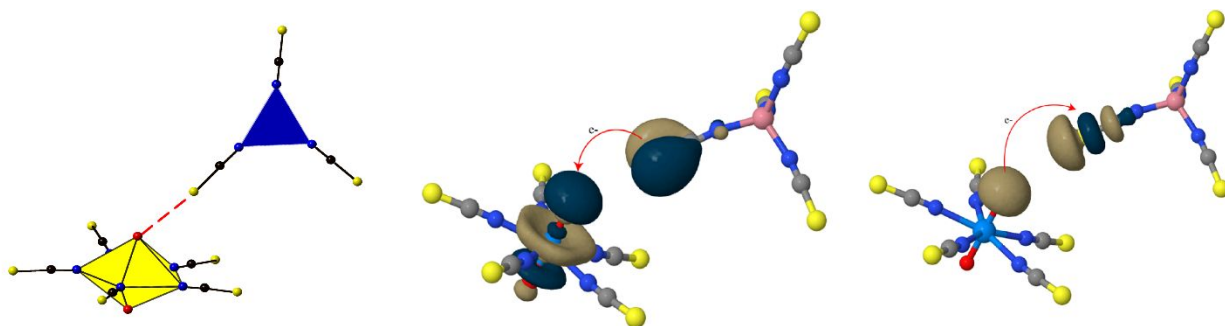
Figure 11: Left: Observed S···O_{yl} interaction present in the heterometallic phase **3**. Middle: NLMOs involved in forward S···O_{yl} interaction where S lone pair electrons are donated to acceptor U=O σ* orbitals. Right: NLMO of O lone pair back donation to S-C antibonding orbitals (**SI Figures S31-S32, SI Table S14**).

Natural Bond Orbital and Wiberg Bond Order Analysis. Whereas SOPT allowed for the determination of specific molecular orbital involvement in NCIs, we used NBO and natural localized molecular orbital (NLMO) analysis to interrogate bonding *within* the first coordination sphere of the U atom. NLMO calculations provide the atomic orbitals involved in bonding and are able to confirm that the U=O bond is *weakened* by S···O_{yl} interactions as indicated by frequency and SOPT calculations. Inspired by the work of Hayton[12,84] and others,[13,24,79,85,86] we quantify U=O bond strength as a function of percent parent atom character within bonding interactions. From this analysis the percent parent atom character of the U-O bonds (U-O1 and U-O2) was extracted (**Table 3**). For our purposes, a higher metal percentage within metal-ligand bonding is expected to correlate to a stronger, more covalent interaction between the two atoms.[84]

Table 3: Parent atom contributions to U=O bonding in homo- and heterometallic models, derived from NLMO analysis, comparing %U and %O of bonding interactions. Relevant U=O bonding orbitals are rendered and assigned as either σ or π (**SI Figures S18-S20**).

$$\begin{array}{c} \cdot^{\cdot\cdot\cdot} SCN \\ O_2 \\ \| \\ U \\ \| \\ O_1 \end{array}$$
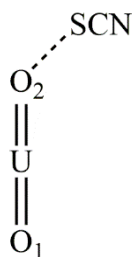
Bond	Bond Type	Homometallic U=O		Heterometallic U=O	
		% U	% O	% U	% O
U-O1	σ	29.92	68.17	28.85	69.33
U-O1	π	21.33	78.34	21.02	78.63
U-O1	π	21.24	78.42	21.02	78.61
U-O2	σ	29.77	68.33	29.93	68.19
U-O2	π	21.25	78.42	21.76	77.89
U-O2	π	21.37	78.28	21.68	77.99
Average	σ	29.85	68.25	29.39	68.76
Average	π	21.30	78.37	21.37	78.28

The %U character in **1** is on average 29.85% for the U-O σ bond and 21.30% for the U-O π bonds. The U-O1 and U-O2 bonds for the homometallic model are highly symmetric, as expected, showing negligible difference in percent parent atom character. This symmetry appears to be subtly disrupted in the case of the heterometallic model which shows minor changes in %U character of U-O σ bonds from 28.85% to 29.93%, and an average U-O π bond increase from 21.02% % to 21.72%. The moderately lower %U character of the U-O1 σ bond of the heterometallic model may be indicative of slight U=O σ bond *weakening* upon formation of S⋯O_{yl} interactions, while the U-O2 bond remains relatively unchanged.

Concurrently, changes in the U *d* and *f* hybridization, extracted from NBO in a similar manner, were used to compare the σ and π components of uranyl bonding (**Table 4**). In both the homo- and heterometallic models the U-O σ bonds consistently feature greater U *f* than *d*

contributions, with U-O π bonds showing larger relative U d character. The U-O1 and U-O2 bonds in the homometallic model are again symmetric, showing similar %d and %f character. When interrogating the hybridization of atomic orbitals in the heterometallic case, however, one notes a similar, albeit slight, asymmetry in U-O1 and U-O2 bonds as was observed with percent parent atom character. This minor increase in %d character of U-O2 bonds, coupled with an equivalent decrease in %f character, may be due to subtle enhancement of U $6d$ orbitals' involvement in bonding with subsequent $5f$ suppression. This slight asymmetry is again noted simply to show that the introduction of the S$\cdots$O$_{yl}$ interaction does not influence the U-O bonds equally.

Table 4: Comparative d/f hybridization of U atomic orbitals involved in U=O σ- and π-bonding interactions within the $[UO_2(NCS)_5]^{3-}$ anion, as well as the homo- and heterometallic models, derived from NLMO analysis.

$$\begin{array}{c}
\text{SCN} \\
\text{O}_2 \\
\| \\
\text{U} \\
\| \\
\text{O}_1
\end{array}$$
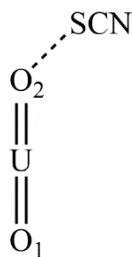
Bond	Bond Type	$[UO_2(NCS)_5]^{3-}$		Homometallic U=O		Heterometallic U=O	
		%6d	%6f	%6d	%5f	%6d	%5f
U-O1	σ	17.39	82.14	17.09	82.44	17.00	82.61
U-O1	π	37.67	62.20	37.66	62.21	37.20	62.69
U-O1	π	37.66	62.21	37.86	62.00	37.50	62.38
U-O2	σ	17.28	82.26	17.09	82.44	17.62	81.90
U-O2	π	37.62	62.25	37.66	62.21	37.89	61.97
U-O2	π	37.53	62.34	37.86	62.00	37.88	61.98
Average	σ	17.34	82.20	17.09	82.44	17.31	82.26
Average	π	37.62	62.25	37.76	62.11	37.62	62.26

Whereas the changes in %U and atomic orbital hybridization suggest U=O bond strength differences between homo- and heterometallic species, as well as subtle asymmetry in the heterometallic model, we decided to explore these findings further by performing Wiberg bond order analysis of both models (**Table 5**). The Wiberg bond order is a measure of electron population overlap between two atoms and is a function of the atomic orbitals and the density matrix element.[87] This method serves as a convenient metric of bond strength, where higher Wiberg bond orders equate to greater orbital overlap, i.e. stronger bonds. In the calculations performed, we note for a third time, a subtle asymmetric effect when $S \cdots O_{yl}$ interactions are present. In the heterometallic model the Wiberg bond indices for the U-O1 and U-O2 bonds are 2.057 and 2.103, respectively. Yet again the heterometallic U-O2, which participates in $S \cdots O_{yl}$ NCIs, is moderately stronger than the nonparticipating U-O1, which appears to be slightly weaker. When taken as an average, however, we note minor bond weakening in the heterometallic compared to the homometallic phase. This slight weakening agrees with our experimental results and previous published findings,[17-21] yet again contrasts what is observed spectroscopically, since a weaker U=O bond should serve to *red shift* the symmetric stretching frequency.

Table 5: B3LYP calculated Wiberg bond indices for U=O bonding within the $[UO_2(NCS)_5]^{3-}$ anion, as well as homometallic and heterometallic models.

Bond	$[UO_2(NCS)_5]^{3-}$	Homometallic	Heterometallic
U-O1	2.080	2.089	2.057
U-O2	2.080	2.082	2.103
Average	2.080	2.086	2.080

Contrary to our Raman v_1 symmetric stretching frequency *blue shifting* between the homo- and heterometallic phases, our computational findings confirm that $S \cdots O_{yl}$ interactions may marginally weaken the U=O bond. Since there is no evidence of other effects at play, for example U=O bond

strengthening, it is fair to then conclude that this *blue shift* is due to the influence of normal mode coupling, which is predicted by calculated frequencies. As we have noted, the criteria of U=O and U-NCS coupling is met in all cases yet is only observed in the heterometallic frequency calculations. We postulate that the introduction of S$\cdots$O$_{yl}$ interactions enables coupling, either by (a) shifting the U=O stretch to lower energies, allowing for a better energy match, or (b) reducing symmetry of the complex increases the number of vibrations that can be coupled. As typical discussions of the uranyl rely heavily on using the ν_1 stretching frequency alone as a comparative measure of U=O bond strength, this finding reveals a limitation in this correlation.

Conclusions

We have reported a family of uranyl and/or cobalt isothiocyanate materials, in which [UO$_2$(NCS)$_5$]$^{3-}$ and [Co(NCS)$_4$]$^{2-}$ anions are paired with TMA$^+$. In doing so, we have assigned assembly criteria for these materials as a function of best donor and acceptor sites as defined by ESP values. In compounds **1-3**, NCIs present in homometallic phases (S$\cdots$S or S$\cdots$N) are outcompeted by S$\cdots$O$_{yl}$ interactions when the heterometallic phase is formed. Upon –yl engagement, we note an unexpected *blue shift* in the uranyl symmetric stretch frequency. By combining our experimental results with a theoretical approach, we were able to pinpoint coupling between U=O and U-NCS stretching modes as the culprit for the atypical blue shift. This coupling is likely caused by either (a) red shifting of U=O stretching frequencies, allowing for a better energy match in the heterometallic phase, or (b) a decrease in symmetry which allows for coupling. We have also provided evidence for minor, yet asymmetric perturbation of –yl bonding, where the U=O bond participating in NCIs is marginally strengthened at the expense of the trans O atom. The overall effect, however, is a modest weakening of the average U=O bond. These findings

highlight important limitations in using U=O stretching frequencies alone to qualify bond strength. As such, future work will focus on tailoring chemistry about the equatorial plane and/or secondary anion species, to determine best practices for "priming the pump" to engage the –yl oxygen, as well as the implications of any observed coupling on spectroscopic behavior.

Associated Content

Electronic Supporting Information

The Electronic Supporting Information is available free of charge on the RSC website. Crystallographic information on CCDC 2078154-2078160 can be obtained free of charge by e-mailing data_request@ccdc. cam.ac.uk or by contacting The Cambridge Crystallographic Data Centre, 12 Union Road, Cambridge, CB2 1EZ UK; Fax +44(0)1223-336033; http://www.ccdc.cam.ac.uk/data_reque st/cif.

> Description of crystallographic structures, other uranyl or cobalt homometallic phase information, PXRD data, Raman spectra, UV-Vis-DRS spectra, and IR spectra of compounds **1-3**. NBO and SOPT tables. (PDF)
> Video of atomic displacement for Raman stretch in homometallic model at 925 cm^{-1} (AVI)
> Video of atomic displacement for Raman stretch in heterometallic model at 877 cm^{-1} (AVI)
> X-ray data for compound **1** (CIF)
> X-ray data for compound **2** (CIF)
> X-ray data for compound **3** (CIF)

Author Information

*Christopher L. Cahill - Department of Chemistry, The George Washington University, Washington, DC 20052, United States; orcid.org/0000-0002-2015-3595;
Email: cahill@gwu.edu

Authors

Nicole M. Byrne - Department of Chemistry, The George Washington University, Washington, DC 20052, United States; orcid.org/0000-0003-0553-5373;
Email: nbyrne@gwu.edu

Mark H. Schofield - Department of Chemistry, The George Washington University, Washington, DC 20052, United States; orcid.org/0000-0002-9601-7186;

32

Email: mschofie@gwu.edu

Aaron D. Nicholas - Department of Chemistry, The George Washington University, Washington, DC 20052, United States; orcid.org/0000-0001-9003-2126; Email: aaron_nicholas@gwu.edu

Conflicts of Interest

There are no conflicts to declare.

Acknowledgements

References

1. M. B. Andrews and C. L. Cahill, "Uranyl Bearing Hybrid Materials: Synthesis. Speciation, and Solid-State Structures." *Chem. Rev.*, 2013, **113**, 1121-1136.

2. R. C. Severance, S. A. Vaughn, M. D. Smith, and H. C. zur Loye, "Structures and Luminescent Properties of New Uranyl-Based Hybrid Materials." *Solid State Sci.*, 2011, **6**, 1344-1353.

3. P. Thuery, Y. Atoini, and J. Harrowfield, "Structure-Directing Effects of Counterions in Uranyl Ion Complexes with Long-Chain Aliphatic α,ω-Dicarboxylates: 1D to Polycatenated 3D Species" *Inorg. Chem.*, 2019, **58**, 567-580.

4. W. Yang, S. Dang, H. Wang, T. Tian, Q. J. Pan, and Z. M. Sun, "Synthesis, Structures, and Properties of Uranyl Hybrids Constructed by a Variety of Mono- and Polycarboxylic Acids." *Inorg. Chem.*, **52**, 12394-12402.

5. J. Ding, C. Zheng, L. Wang, C. Lu, B. Zhang, Y. Chen, M. Li, G. Zhai, and X. Zhuang, "Viologen-Inspired Functional Materials: Synthetic Strategies and Applications." *J. Mater. Chem. A*, 2019, **7**, 23337-23360.

6. R. G. Surbella III and C. L. Cahill, "Hybrid Materials of the f-Elements Part II: The Uranyl Cation." *Handbook on the Physics and Chemistry of Rare Earths*, Elsevier, 48, 2015, 276 163-285.

7. K. P. Carter, R. G. Surbella III, M. Kalaj, and C. L. Cahill, "Restricted Speciation and Supramolecular Assembly in the 5f Block." *Chem. Eur. J.*, 2018, **24**, 12747-12756.

8. R. G. Surbella III, L. C. Ducati, K. L. Pellegrini, B. K. McNamara, J. Autschbach, J. M. Schwantes, and C. L. Cahill, "Transuranic Hybrid Materials: Crystallographic and Computational Metrics of Supramolecular Assembly." *J. Am. Chem. Soc.*, 2017, **139**, 10843-10855.

9. N. P. Deifel and C. L. Cahill, "The Uranyl Tetrachloride Anion as an Anion in the Assembly of U(VI) Hybrid Materials." *CrystEngComm,* 2009, **12**, 2739-2744.

10. G. Liu, N. P. Deifel, C. L. Cahill, V. V. Zhurov, and A. A. Pinkerton, "Charge Transfer Vibronic Transitions in Uranyl Tetrachloride Compounds." *J. Phys. Chem.,* 2012, **116**, 855-864.

11. J. A. Platts and R. J. Baker, "Non-Covalent Interactions of Uranyl Complexes: A Theoretical study." *Phys. Chem. Chem. Phys.*, 2018, **20**, 15380.

12. S. Fortier and T. W. Hayton. "Oxo Ligand Functionalization in the Uranyl Ion (UO_2^{2+})" *Coord. Chem. Rev.*, 2010, **254**, 197-214.

13. M. J. Sarsfield and M. Helliwell, "Extending the Chemistry of the Uranyl Ion: Lewis Acid Coordination to a U=O Oxygen." *J. Am. Chem. Soc.*, 2004, **126**, 1036-1037.

14. P. L. Arnold, A. F. Pecharman, R. M. Lord, G. M. Jones, E. Hollis, G. S. Nichol, L. Maron, J. Fang, T. Davin, and J. B. Love, "Control of Oxo-Group Functionalization and Reduction of the Uranyl Ion." *Inorg. Chem.*, 2015, **54**, 3702-3710.

15. A. J. Lewis, H. Yin, P. J. Carroll, and E. J. Schelter, "Uranyl-Oxo Coordination Directed by Non-Covalent Interactions." *Dalton Trans.*, 2014, **43**, 10844-10851.

16. L. A. Watson and B. P. Hay, "Role of the Uranyl Oxo Group as a Hydrogen Bond Acceptor." *Inorg. Chem.*, 2011, **50**, 2599-2605.

17. K. P. Carter, M. Kalaj, R. G. Surbella III, L. C. Ducati, J. Autschbach, and C. L. Cahill, "Engaging the Terminal: Promoting Halogen Bonding Interactions with Uranyl Oxo Atoms." *Chem. Eur. J.*, 2017, **23**, 15355-15369.

18. K. P. Carter, M. Kalaj, A. Kerridge and C. L. Cahill, "Probing Hydrogen and Halogen-Oxo Interactions in Uranyl Coordination Polymers: A Combined Crystallographic and Computational Study." *CrystEngComm*, 2018, **20**, 4916.

19. M. Kalaj, K. P. Carter and C. L. Cahill, "Isolating Equatorial and Oxo Based Influences on Uranyl Vibrational Spectroscopy in a Family of Hybrid Materials Featuring Halogen Bonding Interactions with Uranyl Oxo Atoms." *Eur. J. Inorg. Chem.*, 2017, **21**, 4702-4713.

20. T. S. Franczyk, K. R. Czerwinski and K. N. Raymond, "Sterognostic Coordination Chemistry. 1. The Design and Synthesis of Chelators for the Uranyl Ion" *J. Am. Chem. Soc.*, 1992, **114**, 8138-8146.

21. J. A. Ridenour, M. H. Schofield and C. L. Cahill, "Structural and Computational Investigation of Halogen Bonding Effects on Spectroscopic Properties within a Series of Halogenated Uranyl Benzoates" *Cryst. Growth Des.*, 2020, **2**, 1311-1318.

22. R. G. Surbella III, L. C. Ducati, J. Autschbach, N. P. Deifel and C. L. Cahill, "Thermochromic Uranyl Isothiocyanates: Influencing Charge Transfer Bands with Supramolecular Structure." *Inorg. Chem.*, 2018, **57**, 2455-2471.

23. R. G. Surbella III and C. L. Cahill, "The Exploration of Supramolecular Interactions Stemming from the $[UO_2(NCS)_4(H_2O)]^{-2}$ Anion and Substituted Pyridinium Cations." *CrystEngComm*, 2014, **16**, 2352-2364.

24. S. Nuzzo, B. Twamley, J. A. Platts and R. J. Baker, "Pseudohalide Tectons within the Coordination Sphere of the Uranyl Ion: Experimental and Theoretical Study of C-H⋯O, C-H⋯S, and Chalcogenide Non-covalent Interactions." *Inorg. Chem.*, 2018, **57**, 3699-3712.

25. C. E. Rowland, M. G. Kanatzidis and L. Soderholm, "Tetraalkylammonium Uranyl Isothiocyantes." *Inorg. Chem.*, 2012, **51**, 11798-11804.

26. E. Hashem, J. A. Platts, F. Hartl, G. Lorusso, M. Evangelisti, C. Schulzke and R. J. Baker, "Thiocyanate Complexes of Uranium in Multiple Oxidation States: A Combined Structural, Magnetic, Spectroscopic, Spectroelectrochemical, and Theoretical Study." *Inorg. Chem.*, 2014, **53**, 8624-8637.

27. N. Aoyagi, K. Shimojo, N. R. Brooks, R. Nagaishi, H. Nagnawa, K. Van Hecke, L. Van Meervelt, K. Binnemans and T. Kimura, "Thermochromic Properties of Low-Melting Ionic Uranyl Isothiocyanate Complexes." *Chem. Commun.*, 2011, **47**, 4490-4492.

28. J. C. Berthet, P. Theury and M. Ephritikhine, "The First Actinyl Cyanide." *Chem. Commun.*, 2007, 604-606.

29. T. Dumas, D. Guillaumont, P. Moisy, D. K. Shuh, T. Tyliszczak, P. L. Solari and C. Den Auwer, "The Electronic Structure of f-Element Prussian Blue Analogs Determined by Soft X-ray Absorption Spectroscopy." *Chem. Commun.*, 2018, **54**, 12206.

30. S. Biswas, S. Ma, S. Nuzzo, B. Twamley, A. T. Russell, J. A. Platts, F. Hartl and R. J. Baker, "Structural Variability of 4f and 5f Thiocyanate Complexes and Dissociation of Uranium(III)-Thiocyanate Bonds with Increased Ionicity." *Inorg. Chem.*, 2017, **56**, 14426-14437.

31. S. Nuzzo, M. P. Browne, B. Twamley, M. E. G. Lyons and R. J. Baker, "A Structural and Spectroscopic Study of the First Uranyl Selenocyanate, [Et$_4$N]$_3$[UO$_2$(NCSe)$_5$]" *Inorganics*, 2016, **4**.

32. P. Cauliez, V. Polo, T. Toisnel, R. Llhusar and M. Formigue, "The Thiocyanate Anion as a Polydentate Halogen Bond Acceptor." *CrystEngComm*, 2010, **12**, 558-566.

33. C. Glidewell, "Reactions of Thiocyanate Ions with Acid." *J. Chem. Educ.*, 1984, **61**, 78.

34. M. M. Botz, "Processes for the Regeneration of Cyanide from Thiocyanate." *Miner. Metall. Process.*, 2001, **16**, 3.

35. R. Rich *Inorganic Reactions in Water*, Springer-Verlag Berlin Heidelberg, 2007.

36. E. Shurdha, C. E. Moore, A. L. Rheingold, S. H. Lapidus, P. W. Stephens, A. M. Arif and J. S. Miller, "First Row Transition Metal (II) Thiocyanate Complexes, and Formation of

1-, 2-, and 3-Dimensional Extended Network Structures of M(NCS)$_2$(Solvent)$_2$ (M= Cr, Mn, Co) Composition." *Inorg. Chem.*, 2013, **52**, 10583-10594.

37. Bruker, APEXIII, Bruker AXS Inc., Madison, Wisconsin, USA., 2020.

38. Bruker, BIS, Bruker AXS Inc., Madison, Wisconsin, USA, 2020.

39. Bruker, *SAINT*, Bruker AXS Inc., Madison, Wisconsin, USA., 2020.

40. Bruker, *SADABS*. Bruker AXS Inc., Madison, Wisconsin, USA., 2020.

41. Bruker, *TWINABS*. Bruker-AXS Inc., Madison, Wisconsin, USA 2012.

42. G. M. Sheldrick "SHELXT – Integrated Space-group and Crystal-structure Determination" *Acta. Cryst.*, 2015, **A71**, 3-8.

43. J. Lubben, C. M. Wandtke, C. B. Hubschle, M. Ruf and G. M. Sheldrick, "Aspherical Scattering Factors for SHELXL – Model, Implementation and Application" *Acta. Cryst.,* 2019, **A78**, 50-62.

44. O. V. Dolomanov, L. J. Bourhis, R. J. Gildea, J. A. K. Howard and H. Puschmann, *J. Appl. Cryst.*, 2009, **42**, 339-341.

45. A. L. Spek, "Structure Validation in Chemical Crystallography" *Acta. Cryst.*, 2009, **D65**, 148-155.

46. C. F. Macrae, P. R. Edgington, P. McCabe, E. Pidcock, G. P. Shields, R. Taylor, M. Towler, J. van de Streek. "Mercury: Visualization and Analysis of Crystal Structures." *J. Appl. Cryst.*, 2006, **39**, 453-457.

47. D. C. Palmer, CrystalMaker 8.2, CrystalMaker Software Ltd., Begbroke, Oxfordshire, England, 2014.

48. H. Putz and K Brandenburg GbR, Match! – Phase Analysis using Powder Diffraction, Crystal Impact, Bonn, Germany, 2020.

49. M. Wojdyr, "*Fityk*: A General-Purpose Peak Fitting Program". *J. Appl. Cryst.,* 2010, **43**, 1126-1128.

50. M. J. Frisch, G. W. Trucks, H. B. Schlegel, G. E. Scuseria, M. A. Robb, J. R. Cheeseman, G. Scalmani, V. Barone, G. A. Petersson, H. Nakatsuji, X. Li, M. Caricato, A. V. Marenich, J. Bloino, B. G. Janesko, R. Gomperts, B. Mennucci, H. P. Hratchian, J. V. Ortiz, A. F. Izmaylov, J. L. Sonnenberg, D. Williams-Young, F. Ding, F. Lipparini, F. Egidi, J. Goings, B. Peng, A. Petrone, T. Henderson, D. Ranasinghe, V. G. Zakrzewski, J. Gao, N. Rega, G. Zheng, W. Liang, M. Hada, M. Ehara, K. Toyota, R. Fukuda, J. Hasegawa, M. Ishida, T. Nakajima, Y. Honda, O. Kitao, H. Nakai, T. Vreven, K. Throssell, J. A. Montgomery, Jr., J. E. Peralta, F. Ogliaro, M. J. Bearpark, J. J. Heyd, E. N. Brothers, K. N. Kudin, V. N. Staroverov, T. A. Keith, R. Kobayashi, J. Normand, K. Raghavachari, A. P. Rendell, J. C. Burant, S. S. Iyengar, J. Tomasi, M. Cossi, J. M. Millam, M. Klene, C. Adamo, R. Cammi, J. W. Ochterski, R. L. Martin, K. Morokuma, O. Farkas, J. B. Foresman and D. J. Fox, Gaussian 16 (Revision C.01), Gaussian, Inc., Wallingford CT, 2016.

51. E. D. Glendening, J. K. Badenhoop, A. E. Reed, J. E. Carpenter, J. A. Bohmann, C. M. Morales, P. Karafiloglou, C. R. Landis and F. Weinhold, NBO 7.0, Theoretical Chemistry Institute, University of Wisconsin, Madison, 2018.

52. F. Weinhold and C. R. Landis, "Natural Bond Orbitals and Extensions of Localized Bonding Concepts" *Chem. Educ. Res. Pract.*, 2001, **2**, 91-104.

53. E. D. Glendening, C. R. Landis and F. Weinhold, "Natural Bond Orbital Methods." *WIREs Comput. Mol. Sci.*, 2012, **2**, 1-42.

54. W. Kuechle, M. Dolg, H. Stoll and J. Preuss, "Energy-Adjusted Pseudopotentials for the Actinides. Parameter Sets and Test Calculations for Thorium and Thorium Monoxide." *J. Chem. Phys.*, 1994, **100**, 7535.

55. X. Cao, M. Dolg and H. Stoll, "Valence Basis Sets for Relativistic Energy-Consistent Small-Core Actinide Pseudopotentials." *J. Chem. Phys.*, 2003, **118**, 487.

56. X. Cao and M. Dolg, "Segmented Contraction Scheme for Small-Core Actinide Pseudopotential Basis Sets." *J. Molec. Struct. (Theochem)*, 2004, **673**, 203.

57. R. Dennington, T. A. Keith, J. M. Millam, GaussView (Version 6), Semichem Inc., Shawnee Mission, KS, 2016.

58. Avogadro: An Open-source Molecular Builder and Visualization Tool. Version 1.2.0. http://avogadro.cc/

59. M. D. Hanwell, D. E. Curtis, D. C. Lonie, T. Vandermeersch, E. Zurek and G. R. Hutchison, "Avogadro: An Advanced Semantic Chemical Editor, Visualization, and Analysis Platform" *J. Cheminf.*, 2012, **4**.

60. Jmol: An Open-source Java Viewer for Chemical Structures in 3D. http://www.jmol.org/

61. A. A. Bagabas, M. Alsawalha, M. Sohail, S. Alhoshan and R. Arasheed, "Synthesis, Crystal Structure, and Characterization of Cyclohexylammonnium Tetraisothiocyanatocobaltate(II): A Single-Source Precursor for Cobalt Sulfide and Oxide Nanostructures." *Heliyon*, 2019, **5**, 2405.

62. S. Han, S. L. Dai, W. Q. Chen, J. R. Zhou, L. M. Yang and C. L. Ni, "Complicated Weak Interactions in a Hybrid Material Containing Tetra(isothiocyanate)cobalt(II) and 1,1'-ethylene-2,2'-dipyridinium: Synthesis, Crystal Structure, and Magnetic Properties." *J. Coord. Chem.*, 2012, **15**, 2751-2761.

63. H. Q. Ye, L. J. Su, X. X. Chen, X. Liao, Q. T. Liu, X. Y. Wu, J. R. Zhou, L. M. Yang and C. L. Ni, "Syntheses, Crystal Structures, Weak Interaction, Magnetic, and Luminescent Properties of Two New Organic-Inorganic Molecular Solids with Substituted Chlorobenzyl Triphenylphosphinium and Tetra(isothiocyanate)cobalt(II) Anion." *Synth. Met.*, 2015, **199**, 232-240.

64. Y. Jie, Y. Huang, Z. YouQuan, F. Ting, H. Fan, K. Qian and Y. H. Ye, "Synthesis, Crystal Structure, and Magnetic Properties of the Complex $[(CH_3NH)_3]_2[Co(NCS)_4]$" *Z. Naturforch,* 2018, **73**, 571-575.

65. G. Cavallo, P. Metrangolo, R. Milani, T. Pilati, A. Priimagi, G. Resnati and G. Terraneo, "The Halogen Bond." *Chem. Rev.*, 2016, **116**, 2478-2601.

66. K. T. Mahmudov, M. N. Kopylovich, M. F. C. Guedes da Silva, A. J. L. Pombiero, "Chalcogen Bonding in Synthesis, Catalysis and Design of Materials." *Dalton Trans.*, 2017, **46**, 10121.

67. T. Kusamoto, H. M. Yamamoto and R. Kato, "Utilization of σ-Holes on Sulfur and Halogen Atoms for Supramolecular Cation⋯Anion Interactions in Bilayer $Ni(dmit)_2$ Anion Radical Salts." *Cryst. Growth Des.*, 2013, **13**, 4533-4541.

68. R. Gleiter, H. Gebhard, D. B. Werz, F. Rominger and C. Bleiholder*,* "From Noncovalent Chalcogen-Chalcogen Interactions to Supramolecular Aggregates: Experiments and Calculations." *Chem. Rev.*, 2018, **118**, 2010-2041.

69. I. S. Antonijevic, G. V. Janjic, M. K. Milcic and S. D. Zaric, "Preferred Geometries and Energies of Sulfur-Sulfur Interactions in Crystal Structures." *Cryst. Growth Des.*, 2016, **16**, 632-639.

70. A. Bondi, "van der Waals Volumes and Radii." *J. Phys. Chem.*, 1964, **68**, 441-451.

71. M. Borovina, I. Kodrin and M. Dakovic, "Predicting Supramolecular Connectivity of Metal-Containing Solid-State Assemblies Using Calculated Molecular Electrostatic Potential Surfaces." *Cryst. Growth Des.*, 2019, **19**, 1985-1995.

72. M. D. Perera, J. Desper, A. S. Sinha and C. B. Aakeroy, "Impact and Importance of Electrostatic Potential Calculations for Predicting Structural Patterns of Hydrogen and Halogen bonding." *CrystEngComm*, 2016, **18**, 8631.

73. C. B. Aakeroy, C. L. Spartz, s. Dembowski, S. Dwyre and J. Desper, "A Systematic Structural Study of Halogen Bonding Versus Hydrogen Bonding within Competitive Supramolecular Systems." *IUCrJ,* 2015, **2**, 498-510.

74. C. B. Aakeroy, T. K. Wijethunga and J. Desper, "Molecular Electrostatic Potential Dependent Selectivity of Hydrogen Bonding." *New J. Chem.*, 2015, **39**, 822-828.

75. J. Bernstein, M. C. Etter and L. Leiserowitz, "The Role of Hydrogen Bonding in Molecular Assemblies." *Struct. Correl.*, 1994, 431-507.

76. N. B. Figgis, *Introduction to Ligand Fields*, Wiley, New York, 1966.

77. S. J. Osborne, S. Wellens, C. Ward, S. Felton, R. M. Bowman, K. Binnemans, M. Swadzba-Kwasny, H. Q. Nimal Gunartne and P. Nockemann, "Thermochromism and Switchable Paramagnetism of Cobalt(II) in Thiocyanate Ionic Liquids." *Dalton Trans.*, 2015, **44**, 11286-11289.

78. G. Miessler and P. J. Tarr, *Inorganic Chemistry*, Pearson, 5, 2014.

79. G. Lu, A. J. Haes and T. Z. Forbes, "Detection and Identification of Solids, Surfaces, and Solutions of Uranium Using Vibrational Spectroscopy." *Coord. Chem. Rev.*, 2018, **374**, 314-344.

80. P. Di Pietro and A. Kerridge, "U-O$_{yl}$ Stretching Vibrations as a Quantitative Measure of the Equatorial Bond Covalency in Uranyl Complexes: A Quantum Chemical Investigation." *Inorg. Chem.*, 2016, **55**, 573-583.

81. P. Di Pietro and A. Kerridge, "Assessing Covalency in Equatorial U-N Bonds: Density Based Measures of Bonding in BTP and Isoamethryin Complexes of Uranyl." *Phys. Chem. Chem. Phys.*, 2016, **18**, 16830-16839.

82. S. Tsushima, "On the 'yl' Bond Weakening in Uranyl(VI) Coordination Complexes." *Dalton Trans.*, 2011, **40**, 6732.

83. J. K. Gibson, W. A. de Jong, M. J. van Stipdonk, J. Martens, G. Berden and J. Oomens, *J. Organomet. Chem.*, 2018, **857**, 94-100.

84. D. E. Smiles, G. Wu, N. Kaltsoyannis and T. W. Hayton, "Equatorial Coordination of Uranyl: Correlating Ligand Charge Donation with the O$_{yl}$-U-O$_{yl}$ Asymmetric Stretch Frequency." *Chem. Sci.*, 2015, **6**, 3891-3899.

85. N. Kaltsoyannis, "Does Covalency Increase or Decrease across the Actinide Series? Implications for Minor Actinide Partitioning" *Inorg. Chem.*, 2012, **52**, 3407-3413.

86. J. Tanti, M. Lincoln and A. Kerridge, "Decomposition of d- and f-Shell Contributions to Uranium Bonding from the Quantum Theory of Atoms in Molecules: Application to Uranium and Uranyl Halides." *Inorganics*, 2018, **6**, 88.

87. K. B. Wiberg, "Application of the Pople-Santry-Sengal CNDO Method to the Cyclopropylcarbinyl and Cyclobutyl Cation and to the Bicyclobutane." *Tetrahedron*, 1966, **24**, 1083-1096.